JACS
JOURNAL OF THE AMERICAN CHEMICAL SOCIETY
Article
pubs.acs.org/JACS

Single Molecular Conductance of Tolanes: Experimental and Theoretical Study on the Junction Evolution Dependent on the Anchoring Group

Wenjing Hong,[†] David Zsolt Manrique,[‡] Pavel Moreno-García,[†,∥] Murat Gulcur,[§] Artem Mishchenko,[†] Colin J. Lambert,*[,‡] Martin R. Bryce,*[,§] and Thomas Wandlowski*[,†]

[†]Department of Chemistry and Biochemistry, University of Bern, Freiestrasse 3, CH-3012 Bern, Switzerland
[‡]Department of Physics, Lancaster University, Lancaster LA1 4YB, England
[§]Department of Chemistry, Durham University, Durham DH1 3LE, United Kingdom
[∥]Instituto de Física, Benemérita Universidad Autónoma de Puebla, Apartado Postal J-48, Puebla 72570, México

Supporting Information

ABSTRACT: Employing a scanning tunneling microscopy based beak junction technique and mechanically controlled break junction experiments, we investigated tolane (diphenylacetylene)-type single molecular junctions having four different anchoring groups (SH, pyridyl (PY), NH_2, and CN) at a solid/liquid interface. The combination of current−distance and current−voltage measurements and their quantitative statistical analysis revealed the following sequence for junction formation probability and stability: PY > SH > NH_2 > CN. For all single molecular junctions investigated, we observed the evolution through multiple junction configurations, with a particularly well-defined binding geometry for PY. The comparison of density functional theory type model calculations and molecular dynamics simulations with the experimental results revealed structure and mechanistic details of the evolution of the different types of (single) molecular junctions upon stretching quantitatively.

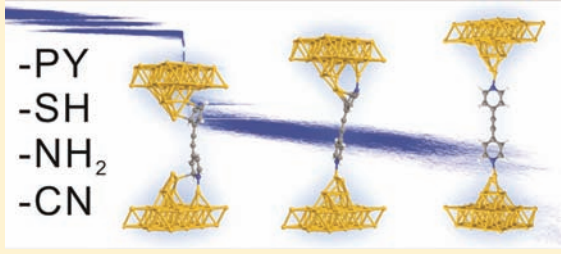

INTRODUCTION

The formation of molecular junctions is a prerequisite for addressing charge transport in molecular components and devices.[1−3] Several approaches have been developed to monitor and to characterize charge transport in nanoscale junctions. They include techniques for formation of molecular junctions[4] such as scanning tunneling microscopy (STM),[5−7] conductive-probe atomic force microscopy (CP-AFM),[8−10] scanning tunneling microscopy break junctions (STM-BJs),[3,11−15] crossed wires,[16] nanoparticle assemblies,[17] mechanically controlled break junctions (MCBJs),[2,18−22] electromigration break junctions (E-BJs),[23,24] nanopores,[25] and liquid metal junctions employing mercury[26,27] or gallium−indium eutectic alloys (EGaIn).[28] A critical issue in all these experimental techniques is the electrical contact between single and/or small ensembles of molecular wires and the macroscopic leads. The ideal molecular anchoring group should form reproducible and mechanically stable contacts with well-defined binding sites. To optimize charge transport, a second essential property is the strong electronic coupling between the ends of the molecule and the macroscopic (metal) electrodes.[29,30] Chemical synthesis offers unique possibilities to tailor anchoring groups to specific contact sites. This strategy is the main topic of the present paper. However, there are also promising alternative approaches which are based on surface grafting via covalent bonds, such as carbon−carbon,[31] metal−carbon,[32] silicon−carbon.[33]

Amino (NH_2), pyridyl (PY), and thiol (SH) groups are the most frequently used "chemical" anchoring groups in charge transport studies of single-molecule junctions because of their rather stable binding to metals (often gold electrodes) as well as their reasonable electrical coupling in nanoscale heterojunctions with contact to macroscopic metal leads. Thiol was the first and still is the most widespread anchoring group in fundamental charge transport studies with single molecular junctions because of its strong binding to many metals, such as gold, copper, and silver.[2,3,36] Charge transport through SH-bound molecular junctions is dominated by hole transport through the highest occupied molecular orbital (HOMO) because this is the closest level to the metal Fermi level.[34,35] Several authors have demonstrated that SH linkers bind to different sites on metal surfaces, such as gold, which often leads to a wide spread in experimentally measured conductances.[12,36,37] Furthermore, the strong covalent bond between SH and in particular gold surfaces leads to distinct changes in the surface crystallography, such as a weakening of the Au−Au spacing between the first and second metal layers,[38] which may

Received: October 27, 2011
Published: December 16, 2011

   dx.doi.org/10.1021/ja209844r | J. Am. Chem.Soc. 2012, 134, 2292−2304

affect the conductance characteristics of such junctions. Venkataraman et al. showed in a series of recent papers that the NH_2 group might be a promising alternative to SH because of its relatively uniform molecular binding geometry.[39,40] Transport through NH_2-terminated metal−molecule−metal junctions is HOMO controlled.[41] Experimental studies with 4,4′-bipyridine suggested that the aromatic PY anchoring group may also form stable and reproducible molecular junctions.[3] However, Quek et al. argue that surface coordination sites and configurations may change upon stretching of a molecular junction.[42] These authors[39,43,44] showed that the charge transport in wires with PY-type anchoring groups is preferentially controlled by the lowest unoccupied molecular orbital (LUMO).[42,43] Additional support for this conclusion was communicated recently in a single-molecule transport study with PY-terminated oligoynes.[45] Our group explored the contact characteristics of the nitrile (CN) anchoring group in a systematic study with biphenyl derivatives. Density functional theory (DFT) based transport calculations suggested that the LUMO represents the main transport channel.[13] Other anchoring groups explored include isonitrile (NC),[29,46] carboxylic acid termini (COOH),[47] nitro (NO_2),[30] trimethyltin ($SnMe_3$),[32] and fullerene.[48,49]

Tao et al. compared conductances of aliphatic molecular wires with COOH, SH, and NH_2 anchoring groups. These authors reported that the junction conductances decrease in the following sequence: SH > NH_2 > COOH.[47] Kushmerick et al. showed in experiments with SH-, PY-, and NO_2-terminated oligo(phenyleneethynylene) (OPE) derivatives that the nature of the anchoring group has a distinct effect on the current rectification.[50] These conclusions are supported by Zotti's calculations with SH, CN, NO_2, and NH_2 anchoring groups[30] and a recent experimental report by Loertscher et al. with NC and SH[29] substituted molecular rods. Both papers are based on an analysis of current (I)−bias voltage (V_{bias}) traces acquired in an MCBJ setup under vacuum conditions. In particular, the electronic coupling at the respective molecule−metal interfaces was investigated.

MCBJ and STM-BJ experiments provide a unique platform for exploring the evolution of molecular contacts during the formation and breaking processes under controlled conditions in a wide parameter space. Many configurations can be sampled and characterized quantitatively on the basis of a statistical analysis of current−distance and/or current−voltage traces. Comparison with ab initio calculations has the potential to extract most probable junction geometries as well as structural changes during the pulling and/or breaking processes.[51,52] Besides the conductance characteristics, the plateau length in current−distance traces provides additional information about the stability and evolution of molecular junctions. At room temperature, the plateau length and stability are dominated by the binding strength of the anchoring group and competition with thermal vibrations. Tao et al. found, on the basis of room temperature STM-BJ studies in toluene, that NH_2-terminated aliphatic wires form longer plateaus, i.e., more stable molecular junctions, than COOH wires.[47] Venkataraman et al. compared amines (NH_2) with dimethylphosphine (PMe_2) and methyl sulfide (SMe) anchoring groups. These authors reported the following stability sequence: PMe_2 > SMe > NH_2.[53,54] Anchor groups with a narrow distribution of binding sites and conformations also provide a unique platform to explore molecular details of the evolution of junction structure and conductance properties during the stretching process. This strategy was explicitly addressed in a comparative experimental work with benzene derivatives having SH-, NH_2-, and NC-terminated contact sites.[39]

Most experimental works to date have focused on the search for and determination of conductance values for specific systems and the comparison of measurements and predictions by different research groups. However, the evolution of a molecular junction during the stretching process was hardly investigated.[42,54−56] The analysis of entire stretching traces is essential for understanding contact geometries, binding configurations, molecular-junction evolution, most probable junction characteristics and their spread, and differences between the results of various experimental approaches. Kruger et al. reported ab initio molecular dynamics (MD) simulations of gold nanowires formed in the presence of chemisorbed thiolates.[55] They demonstrated the formation of monatomic gold nanowires leading to the preferential breaking of Au−Au instead of Au−S bonds during a simulated rupture event. This approach was also used to demonstrate the formation of gold clusters during the stretching process.[57] The result is in agreement with an earlier suggestion.[58] Konopka et al. showed for the copper−alkylthiolate interface that mechanical stress, as typically applied in a molecular junction, stabilizes selectively the S−C bond due to the suppression of fluctuations and undercoordination of the sulfur atom due to a strongly uniaxial stress upon pulling.[59] Very recently, Kim et al. reported in a combined experimental and theoretical study of SH- and NH_2-terminated octanes, bound at low temperatures to gold electrodes, that the SH-terminated molecules cause large deformations of the Au electrode.[60] This effect is much weaker for amine-terminated molecular wires. However, the full simulation of the evolution of molecular configuration changes during the stretching process remains a major challenge.

In this paper we present studies of charge transport during the evolution of single molecular junctions of tolane molecular wires with four terminal end groups, PY, SH, NH_2, and CN (Scheme 1) attached to gold leads. We report complementary

Scheme 1. Structures of the Studied Molecules

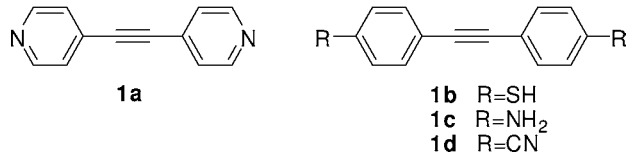

1a

1b R=SH
1c R=NH_2
1d R=CN

experiments in STM-BJs as well as in an MCBJ setup, both in solution and under environmentally controlled conditions. On the basis of a statistical analysis of conductance−distance traces, we have explored the evolution of the four types of single molecular junctions during the stretching process and extracted conductances for different junction geometries and addressed their stability and their probability of formation. We aim to develop an understanding of the entire stretching process in an attempt to evaluate the specifics of the individual anchoring groups in promoting efficient electronic and mechanical coupling to metal electrodes. The relative position of the molecular levels with respect to the Fermi level is extracted from current−voltage curves as recorded simultaneously at various stages of the stretching process. DFT-based calculations reveal the nature of the transport channels involved for selected stable binding geometries. These computations are then extended to yield a simulation of entire conductance versus

dx.doi.org/10.1021/ja209844r | J. Am. Chem.Soc. 2012, 134, 2292−2304

displacement traces. Comparison with experiments in the range from 10 to 10^{-6} G_0 reveals unique details of the structure and stability of the nanoscale molecular junctions during the entire stretching process.

EXPERIMENTAL SECTION

Chemicals and Organic Synthesis. Compounds **1a**,[61] **1c**,[62] and **1d**[63] were synthesized according to literature routes. The acetyl-protected compound **1b**[64] was synthesized by the modification of the literature route. Further details are summarized in the Supporting Information.

Conductance Measurements. The transport characteristics of single molecular junctions were studied using STM-BJ and complementary MCBJ measurements, in solution, at room temperature, and in an argon-protected environment. Typically, a freshly prepared solution containing a 0.1 mM concentration of the respective sample molecule **1a**−**1d** in a mixture of 1,3,5-dimethylbenzene (TMB; Aldrich, p.a.) and tetrahydrofuran (THF; Aldrich, p.a), ratio 4:1 (v/v), was added into the liquid cell. Deprotection of the diacetyl derivative of **1b** was performed in situ by adding 4 equiv of tetrabutylammonium hydroxide (25%, Aldrich, p.a.). We also carried out complementary STM-BJ and MCBJ experiments in the absence of deprotection agents.

The STM-BJ measurements were performed with a modified Molecular Imaging Pico-SPM housed in an all-glass argon-filled chamber following an experimental strategy and data analysis protocols as described in our previous reports.[17,30] In short, the experimental approach is based on the repeated formation and breaking of molecular junctions between a sharp gold STM tip (0.25 mm diameter wires electrochemically etched, 99.999%, Goodfellow, Cambridge, U.K.) and an atomically flat Au(111) disk electrode. The conductance (G)−distance measurements were performed by applying a constant bias voltage V_{bias} between the tip and substrate and recording the corresponding current signal through a linear amplifier stage. The STM tip was typically moving with a rate of 58 nm/s.

The MCBJ experiments are based on the formation and breaking of molecular junctions between a notched, freely suspended gold wire (0.1 mm diameter, 99.999%, Goodfellow), supported on spring steel sheets (10 mm × 30 mm, thickness 0.25 mm) and fixed with a two-component epoxy glue (Stycast 2850 FT with catalyst 9). The sample sheets were positioned between two holders. A Kel-F liquid cell was mounted onto the sample sheet with a Kalrez O-ring. The sample sheet was bent with a pushing rod controlled by the combination of a stepper motor and a piezo stack. The bending was initialized by the stepper motor. Once the measured current reached a value corresponding to 15 G_0, the stepper motor paused and the piezo stack was activated. This strategy could reduce significantly noise contributions from the operation of the stepper motor. After the junction was completely broken, the piezo stack was reset and the rod pushed down by the stepper motor. In the conductance−distance measurements, the typical moving rate of the pushing rod was 100 nm/s, which translates into an opening and respective closing rate for the two leads of about 1−5 nm/s (displacement ratio of 0.01−0.05). Experiments with the CN-terminated tolane **1d** were carried out with 1000 nm/s and a corresponding relative rate of about 50 nm/s for the horizontal movement of the gold wires. All current measurements were performed with a logarithmic I−V converter which operates in a wide dynamic range giving access to conductance measurements from 10 to below 10^{-7} G_0. For further technical and data evaluation details of our MCBJ setup, we refer to a recent paper.[65]

The high mechanical stability of the MCBJ setup also allowed the simultaneous acquisition of current−voltage characteristics during the stretching process. In these experiments, we reduced the piezo speed to 10 nm/s to slow the breaking process and swept V_{bias} continuously from −1 to +1 V with a speed of 40 V/s. We recorded 500 data points for every I−V_{bias} curve and acquired 25 traces per second. Typically, we measured 20−50 individual curves during the various stages of one single breaking half-cycle. The conductance was calculated from the slopes of the linear parts of the I−V_{bias} curves (−0.3 to +0.3 V). Two-dimensional I−V_{bias} histograms of a molecular junction were constructed by evaluating the experimental traces in the surroundings of the most probable conductance G^* from $10^{-0.2}G^*/G_0$ to $10^{+0.2}G^*/G_0$.

Theoretical Details. The electronic and transport calculations of the four tolane derivatives **1a**−**1d** were performed with the ab initio code SMEAGOL,[66,67] which uses the Hamiltonian provided by the DFT code SIESTA,[68] in combination with the nonequilibrium Green function formalism. SIESTA employs nonconserving pseudopotentials to account for the core electrons and a linear combination of pseudoatomic orbitals. SMEAGOL divides the entire nanoscale junction into three parts: the left and the right bulk electrodes simulated by six gold layers grown along the (111) direction and the "extended molecule" that consists of the molecule, surface clusters, and two layers of gold. SMEAGOL uses the Hamiltonian derived from SIESTA to calculate self-consistently the density matrix, the transmission coefficients $T(E)$ of the electrons from the left to the right lead, and the I−V_{bias} characteristics. Further details about the above computation methods, the energy level alignment, and simulations of the conductance versus distance traces are given in the Supporting Information.

EXPERIMENTAL RESULTS

STM-BJ and MCBJ Conductance Measurements. Figure 1 displays typical conductance−distance stretching traces (on the logarithmic scale) as recorded for the PY derivative **1a** in the STM-BJ (Figure 1C) and MCBJ (Figure 1D) setups at a bias potential V_{bias} = 0.10 V. The curves show characteristic quantized conductance steps occurring at integer multiples of $G_0 = 2e^2/h$, the fundamental quantum conductance. Opening the gap results in an elongation of the gold−gold junction and decreases the number of gold atoms in the constriction, which causes the conductance to change by up to ∼1 G_0, where the contact between the tip and Au(111) substrate of the STM-BJ or between the two gold leads of the MCBJ consists of only one gold atom. Subsequently, an abrupt decrease of the current over several orders of magnitude occurs, which is assigned to the "jump out of atomic contact",[42] and additional features are observed at $G < 10^{-3}$ G_0. The curves show well-developed plateaus in the range from 10^{-3} to 10^{-4} G_0 characterized by a slight, but distinct, monotonic decrease in the conductance with stretching distance. This pronounced high-conductance plateau region (H) is followed by up to two additional, less extended steplike features in the conductance traces, which we label M

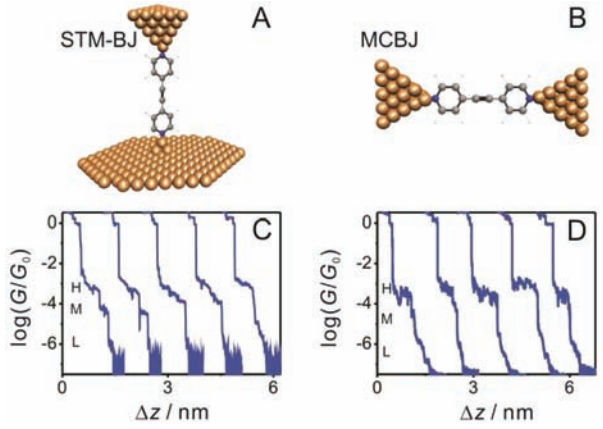

Figure 1. (A, B) Schematics of the of STM-BJ (A) and MCBJ (B) configurations. (C, D) Typical conductance−distance traces of 0.1 mM **1a** (PY) in THF/TMB (1:4, v/v) recorded in the STM-BJ (C) and MCBJ (D) configurations. H, M, and L refer to high, medium, and low conductances, respectively.

dx.doi.org/10.1021/ja209844r | J. Am. Chem.Soc. 2012, 134, 2292−2304

and L, until the noise level is reached. The transitions are not always sequential. We observed traces with plateaus in the H region with either a sharp drop directly into the L region or a drop via the M stage. The features H, M, and L are assigned to molecular junctions bridging the gap between the two gold electrodes. We also note that the noise level is different in the STM-BJ ($G \leq 10^{-6}$ G_0) and MCBJ ($G \leq 10^{-7}$ G_0) measurements because of the different preamplification stages used. Furthermore, due to thermal fluctuations at room temperature, the molecular plateau regions H, M, and L exhibit a certain variation from one trace to another in both experimental configurations, which might reflect different binding geometries and/or switching events between different molecular configurations in the individual stretching traces.

Several thousand individual traces were recorded and subsequently analyzed further by constructing all-data-point histograms without any data selection to extract statistically significant results from the different junction configurations. Figure 2 displays the corresponding one-dimensional (1D)

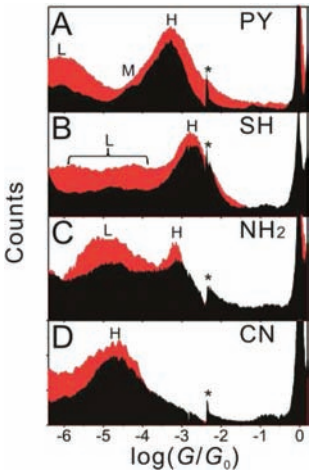

Figure 2. Conductance histogram of (A) PY, (B) SH, (C) NH_2, and (D) CN tolane-type wires from 2000 curves recorded in the STM-BJ (black) or the MCBJ (red) setup. H = high-conductance feature, M = medium-conductance feature, and L = low-conductance feature. The asterisk indicates an experimental artifact originating from switching ranges in our linear amplifier in the STM-BJ setup.

histograms in the logarithmic scale for the four derivatives, constructed from both the experimental STM-BJ (black) and the MCBJ (red) measurements. We observed a clear peak around 1 G_0, which represents the breaking of the last gold–gold atomic contact and a prominent molecular conductance feature H at $10^{-3.3}$ G_0 (PY), $10^{-2.7}$ G_0 (SH), $10^{-3.1}$ G_0 (NH_2), and $10^{-4.6}$ G_0 (CN). Except for the CN derivative **1d**, a second low-conductance peak (L) is clearly resolved for **1a** (PY, $10^{-6.0}$ G_0) and **1c** (NH_2, $10^{-4.8}$ G_0), as well as a more shallow peak for the dithiol derivative **1b**. Here the data scatter between 10^{-4} and 10^{-6} G_0. STM-BJ experiments (black trace in Figure 2B) revealed a broad, single second conductance feature around $10^{-4.7}$ G_0, while two broad maxima could be resolved in the MCBJ setup (red trace) around $10^{-4.2}$ and $10^{-5.8}$ G_0, respectively. As a unique characteristic of **1a**, a third molecular conductance feature M develops between the H and L regions. For the MCBJ the M feature is much less pronounced in the conductance histogram (Figure 2A). Limitations in extracting the characteristic properties of the L region, in particular in the STM-BJ setup with **1a**, could be overcome by complementary MCBJ experiments, which are carried out with a preamplifier stage of higher current sensitivity. The statistically most probable conductance states of the single-molecule junctions formed by **1a–1d** as trapped between the gold contacts were obtained by fitting Gaussians to the characteristic maxima in the conductance histograms. All conductance values (H and L) are summarized in Table 1. They demonstrate nearly perfect

Table 1. Most Probable Conductance Values of 1a–1d from Both MCBJ and STM-BJ Measurements

	H (STM-BJ) $\log(G_H/G_0)$	H (MCBJ) $\log(G_H/G_0)$	L (STM-BJ) $\log(G_L/G_0)$	L (STM) $\log(G_L/G_0)$
1a (PY)	−3.3	−3.3	−6.0	−6.0
1b (SH)	−2.7	−2.7	−4.7	−4.2/-5.8
1c (NH_2)	−3.1	−3.1	−4.8	−4.9
1d (CN)	−4.6	−4.6		

agreement between STM-BJ and MCBJ experiments. The most probable main conductances H decrease in the following sequence: SH > NH_2 > PY ≫ CN. While the values for the first three molecules are rather similar, the CN anchoring group leads to a significantly lower junction conductance for **1d**. The same sequence was observed in recent single-molecule junction conductance studies of substituted biphenyls.[11,13,69] The accessible L data show a similar trend, e.g., SH > NH_2 > PY. However, their values spread over nearly 2 orders of magnitude between 10^{-4} and 10^{-6} G_0. A possible low-conductance feature could not be resolved for the CN-substituted compound **1d** due to masking by instrumental noise.

Two-Dimensional Histograms. The above analysis was extended by constructing two-dimensional (2D) conductance vs displacement histograms.[49] This strategy provides direct access to the evolution of molecular junctions during the formation, stretching, and breakdown steps. The precise calibration of the distance scale in the STM-BJ and MCBJ measurements was carried out by tunneling experiments in the clean solvent. In addition, the piezo movement in the STM setup was scaled with the known height of monatomic steps on the Au(111) surface (d = 0.245 nm). The displacement calibration of the MCBJ traces is performed with the assumption that the tunneling decay is identical to that in an STM-BJ setup under the same experimental conditions.

Parts A–D of Figure 3 display the 2D conductance-versus-displacement histograms[49] of the four tolane derivatives as constructed from 2000 individual STM-BJ traces. The corresponding graphs of the complementary MCBJ measurements are given in the Supporting Information. To assign a common scale to each conductance–distance trace, we have introduced a relative displacement with Δz, defined so that Δz = 0 at 0.1 G_0.[13] This procedure leads to an accurate alignment of the conductance–distance curves because of the sharp drop in conductance at $G < G_0$. The graphs in Figure 3A–D show features in the upper part of the 2D histograms which are attributed to the quantum conductance of gold–gold atomic contacts. Once the gold–gold contact breaks (Δz = 0), the gold atoms snap back quickly by an amount Δz_{corr} estimated as ~0.5 nm (see the Supporting Information for details) and create a nanogap between the two gold electrodes.[70] After adding this correction to the relative displacement, we obtain an absolute displacement $z = \Delta z + \Delta z_{corr}$ which we attribute to the electrode separation. The junctions with molecules trapped

dx.doi.org/10.1021/ja209844r | J. Am. Chem.Soc. 2012, 134, 2292–2304

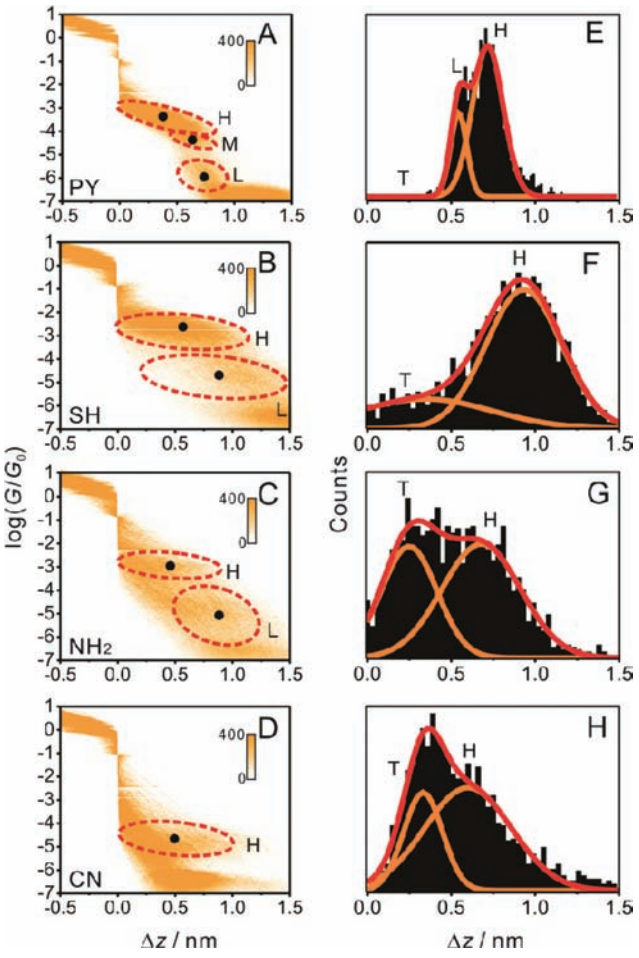

Figure 3. (A–D) 2D conductance–relative displacement histograms from STM-BJ experiments. (E–H) Relative displacement (Δz) distribution from STM-BJ experiments. The relative displacement histograms are obtained from conductance traces between 0.1 and $10^{-3.7}$ G_0 (SH), $10^{-4.0}$ G_0 (NH_2), and $10^{-5.6}$ G_0 (CN). In the case of PY, we consider medium conductances as a subfeature of high conductances and construct relative displacement histograms from conductance traces between 0.1 and $10^{-5.0}$ G_0.

between the adjacent leads undergo several structural changes during the stretching process (i.e., with increasing displacement Δz), which leads to the evolution of distinct data density clouds until the noise level is reached. All tolanes studied reveal clear high-conductance clouds, indicated by the H regions in Figure 3A–D.

In particular, the pyridyl and thiol derivatives **1a** and **1b** show well-defined high-conductance clouds centered on the most probable conductances $10^{-3.3}$ and $10^{-2.7}$ G_0, respectively. The boundaries of the density clouds of the NH_2 ($10^{-2.2}$ to $10^{-4.2}$ G_0) and CN ($10^{-4.2}$ to $10^{-5.5}$ G_0) compounds are less clearly resolved, illustrating that, for these junctions, the percentage of traces which do not lead to molecular junctions is significantly larger. The "smearing out" effect results from the corresponding tunneling-through-solvent traces. As indicated in the 1D histograms of Figure 2, we also observed clear L features for **1a** (10^{-5} to 10^{-6} G_0), **1b** (10^{-4} to 10^{-6} G_0), and **1c** ($10^{-4.5}$ to 10^{-6} G_0) which have never been reported before. No L region was detectable for the CN-terminated tolane, again most probably due to sensitivity limitations of both setups. A medium-conductance region (M) of **1a** is shown in the 1D histograms of Figure 2A and appears in Figure 3A as a small but distinct data density cloud between the H and L states ranging from $\sim 10^{-4}$ to $\sim 10^{-5}$ G_0. Regarding the evolution of the two M and H regions for **1b** (SH) and **1c** (NH_2) and the M, H, and L regions for **1a** (PY), the analysis of the 2D histograms of Figure 3 shows clearly that the H state evolves immediately after breaking of the gold–gold contact, while M and L develop at a later stage during the displacement, at a relative displacement Δz distinctly different from zero. In a comparison with literature data, we notice that molecular junctions of **1a** trapped between two gold electrodes were explored by Wang et al.[45] and Velizhanin et al.[71] using an STM-BJ approach. Their data ($10^{-4.0}$ to $10^{-3.3}$ G_0 and $10^{-3.7}$ to $10^{-3.5}$ G_0) agree within half an order of magnitude with our findings for the M and H states, respectively. However, no evidence was found previously[45,71] for the low-conductance region as discovered in our work. In this context we also mention that two conductance states were also found by Quek et al.[42] for the PY-terminated prototype molecule 4,4′-bipyridine. In a comparative study of dithiolate and carbodithioate linkers, Xing et al.[72] reported a conductance value for **1b** of $10^{-3.6}$ G_0. No suggestion of this value was found in our work. On the other hand, the most probable conductance values, $10^{-3.1}$ and $10^{-3.2}$ G_0, as published in recent papers by Widowsky et al.[73] and Hybertsen et al.[74] for **1c** in 1,2,4-trichlorobenzne are in good agreement with our data for the H state. Finally, we note that Zotti et al. presented I–V_{bias} curves of an MCBJ experiment with **1d**, from which we estimate a low bias junction conductance of $10^{-4.6}$ G_0.

Stretching Distances and Junction Formation Probability. We now analyze the relative-displacement histograms of Figure 3E–H in more detail. The conductance histograms of Figure 2 are obtained by collapsing the 2D data of Figure 3A–D onto the vertical axis. Calculation of the displacement from the relative zero position (0.1 G_0) to the end of the high-conductance feature ($10^{-3.7}$ G_0 (SH), $10^{-4.0}$ G_0 (NH_2), and $10^{-5.6}G_0$ (CN)) of every individual trace yields the relative-displacement distribution histograms of Figure 3E–H. The PY-terminated molecule **1a** develops no stretching traces shorter than 0.3 nm, and the 2D histogram (Figure 3A) does not show features attributed to direct tunneling (T). We conclude that

Table 2. Lengths of Molecular Junctions from DFT Calculations and Experimental Measurements

molecule	L_m(DFT)[a]/nm	Δz^{H*} [b]/nm	$z^{H*} = \Delta z^{H*} + z_{corr}$ [c]/nm	Δz^{L*} [b]/nm	$z^{L*} = \Delta z^{L*} + \Delta z_{corr}$ [c]/nm
PY	1.14	0.7 ± 0.1	1.2 ± 0.2	0.8 ± 0.1	1.3 ± 0.2
SH	1.48	0.9 ± 0.3	1.4 ± 0.4	1.2 ± 0.3	1.7 ± 0.4
NH_2	1.43	0.7 ± 0.2	1.2 ± 0.3	1.0 ± 0.4	1.5 ± 0.5
CN	1.70	0.6 ± 0.3	1.1 ± 0.4		

[a]DFT result for the distance L_m from the center of the bond between the left binding gold atom and the anchor atom closest to the center of the corresponding bond on the right electrode. [b]Estimated from the relative displacement histograms $\log(G/G_0)$ vs Δz. [c]z_{corr} is the snapback distance (see the Supporting Information for details; the error is the standard deviation).

dx.doi.org/10.1021/ja209844r | J. Am. Chem.Soc. 2012, 134, 2292–2304

100% of all stretching traces lead to the successful formation of a single-molecule junction. Upon further displacement Δz, a partial transformation into the M and L states takes place (Figure 3E and Supporting Information). In contrast, the relative-displacement distributions of the molecules with SH, NH_2, or CN termini reveal clear peaks labeled with T around 0.2−0.3 nm which represent contributions from direct tunneling traces (see the Supporting Information). The assignment and discrimination of direct tunneling (T) and molecular junction contributions (H, M, L) were discussed in detail in our previous paper.[13] The peaks marked with L (and H) in Figure 3E−H represent the contribution of true molecular junctions.

The maxima of the relative-displacement distributions, which correspond to the most probable relative displacements Δz^*, are a measure of the most probable plateau length of a molecular junction in a certain conductance range because peaks in the relative-displacement distributions arise from sharp drops in the conductance traces. The values of Δz^* obtained for the H regions (denoted Δz^{H*}) are summarized in Table 2. The SH derivative **1b** gives the highest most probable displacement of 0.9 nm, while the other three molecules, **1a**, **1c**, and **1d**, are characterized by lower values ranging between 0.6 and 0.7 nm. The data for **1a** (PY) (Figure 3E) correspond to both the H and M states with Δz^* = 0.6 nm and Δz^* = 0.7 nm, respectively.

Taking the area ratio between the molecular contributions of the H, M, and L states and the total data density in Figure 3E−H leads to a junction formation probability of the high-conductance state of 90% for the SH-terminated, 60% for the NH_2-terminated, and 70% for the CN-terminated tolane junctions. After the high-conductance junctions break, the junctions transform to the low-conductance state. Extending the analysis of the relative displacement to the entire accessible conductance range between 10^{-1} and 10^{-6} G_0 yields an estimation of the most probable relative displacements Δz^{L*} in the L regions. The trend is similar to that of the H regions, with the longest value of Δz^{L*} for **1b**, which amounts to 1.2 nm, followed by **1c** (1.0 nm) and **1a** (0.9 nm). The numerical values are summarized in Table 2.

For **1a** (PY), as shown in Figure 3E, most of the molecular junctions break at a relative displacement Δz^{L*} of around 0.7 nm. A detailed analysis of the molecular junctions formed (see also the Supporting Information) reveals that 24% of the traces break from the H state and transform to the L state at around 0.5 nm, 22% of the junctions have the transformation at around 0.7 nm, and 54% transform from the H state via the M state into the L state at around 0.7 nm. All the traces ruptured subsequently at around 0.8 nm from the L state. A similar analysis for **1b**−**1d** (Supporting Information, Figure S14) demonstrates that the majority of molecular junctions [(91% (SH), 59% (NH_2), and 70% (CN)] break in the H state with a minor contribution from the respective L state (9% (SH), 41% (NH_2), or 30% (bare tunneling, CN)) without formation of the H state.

Absolute Displacement Scale. The absolute displacement in an experimental molecular junction was estimated by adding the snapback distance upon rupture of the Au−Au monatomic contact to the experimentally measured displacment Δz (Figure 3, Table 2). On the basis of current−displacement traces without trapped molecules, we estimated a snapback distance of Δz_{corr} = 0.5 ± 0.1 nm (for details see the Supporting Information), in agreement with literature data.[42,70] No particular trend of Δz_{corr} was found for the various anchoring groups, and therefore, we use this value as a common correction for all junctions. The corrected most probable absolute displacement z^*= Δz^*+ Δz_{corr} may be considered as an estimate of the electrode separation at which a sharp drop in the conductance occurs.

Adding the snapback distance Δz_{corr} to the relative displacement Δz yields the absolute displacement $z = \Delta z + \Delta z_{corr}$, which is a measure of the electrode separation. The most probable absolute displacements $z^* = \Delta z^* + \Delta z_{corr}$ are listed in Table 2. The values of the most probable absolute displacements z^{H*} for the high-conductance states match the molecular lengths of the SH- and PY-terminated tolanes **1a** and **1b**, which suggests that the most probable breaking of the junction occurs when the molecule is in an upright orientation with respect to the surface normal. The other two derivatives, **1c** and **1d**, possess values of z^{H*} which are lower than their molecular lengths, pointing to a most probable breakage in a tilted orientation. These types of configurations were also analyzed in DFT-based transport calculations with oligo-(phenyleneethynylene) molecular rods.[75] Examination of the junction displacement into the medium-conductance (PY) and low-conductance (PY, SH, and NH_2) regions reveals most probable absolute displacements z^{L*} which are longer than the molecular length, which suggests, in particular for **1a** and **1b**, the pulling out of gold adatoms[57,58,61] and/or the formation of intermolecular π-stacking assemblies.[21,76]

Conductance Decay and Variation with Displacement. The analysis of the 2D histograms and the displacement characteristics provide important information about the evolution of molecular junctions in the H plateau regions and their transition into the M and then L configurations. Venkataraman et al. used the width of the conductance peak to evaluate variations of the binding geometries of SH and NH_2 anchoring groups.[40] However, the peak width also contains contributions from the conductance decay during the stretching process as caused by changes of the tilt and/or torsion angles of the respective molecular rods[75] and evolution of the binding sites. In an attempt to exclude the influence of the conductance decay, we calculated the most probable conductance values as well as the standard derivations from Gaussian fits to cross sections of the 2D histograms at different displacement positions Δz (Figure 4). Compared to the rather constant plateau conductances observed when breaking monatomic metal contacts,[77] the plateaus of molecular junctions extend over much longer distances, with conductance changes during the stretching process of up to 2−3 orders of magnitude. This feature reflects the evolution of molecular orientations and junction configurations during the stretching either in a continuous or in a more steplike regime until complete breakage occurs. As illustrated in Figure 4, the molecules **1a** (PY) and **1c** (NH_2) show a linear conductance decay during the stretching in the H region with slopes of 1.9 and 1.2 $\log(G/G_0)$/nm, respectively. Our stretching simulations (discussed below) suggest that this trend partly reflects the sliding of molecular rods along the electrode surfaces.[42] The dithiol derivate **1b** also exhibits a linear dependence of the conductance on displacement Δz in the H region. However, upon the onset of the transition into the L state, an inflection point develops at around 0.6 nm. At longer displacements, the slope of $|\log(G/G_0)|$ versus Δz increases significantly, which may reflect changes in the Au−S coordination geometry. The CN derivative **1d** also shows an inflection point. However, its

dx.doi.org/10.1021/ja209844r | J. Am. Chem.Soc. 2012, 134, 2292−2304

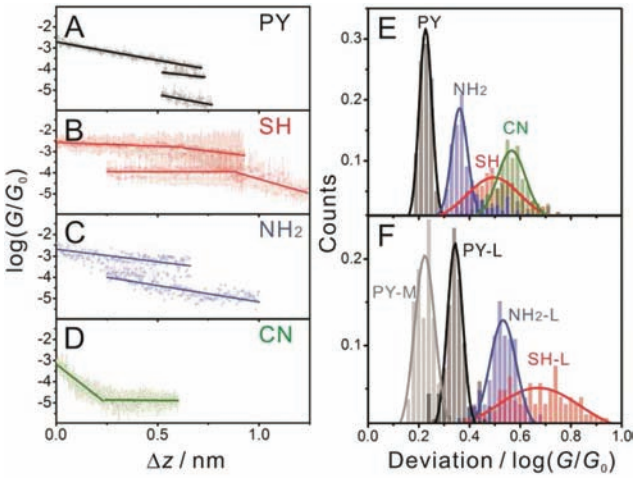

Figure 4. (A–D) Statistically averaged conductance–distance traces (circles) with variation indicated by the standard deviation (bar) and fitting of the traces (line) of PY (A), SH (B), NH_2 (C), and CN (D). (E, F) Distribution of variations in different positions in the (E) H range and (F) M/L range during stretching.

position at around 0.3 nm primarily reflects contributions of "through-space" tunneling at the beginning of the stretching process, which interferes with the molecular junction conductance in this displacement range. Upon increasing the distance between the gold contacts, the additional contribution of the direct tunneling current decreases, and the slope at $\Delta z >$ 0.3 nm is exclusively determined by the conductance through the molecular junction. The statistically averaged conductance–distance traces (Figure 4A–D) show different conductance decays for the four anchor groups, which reflects differences in the evolution of the respective molecular junction configurations during the stretching process. Details of this process will be addressed further in the theory section.

The distributions of conductance-variation histograms shown in Figure 4E were obtained by decomposing the 2D histograms shown in Figure 3 into 1D histograms at different relative displacements Δz. Subsequently, we fitted the main features in the H and L regions with Gaussians to extract the local maximum value of the respective conductance and its variation (i.e., standard deviation) at each relative displacement Δz. The resulting distributions of the variation for all four derivatives in the H region are plotted in Figure 4E. The widths of the distributions of the variations decrease according to the following sequence: PY < NH_2 < SH < CN. Comparison with theory (cf. Figure S16, left column, Supporting Information) suggests that the greater width of the distribution of **1b** reflects the nonuniform binding geometry of the thiol–Au coordination, which may involve 3-fold,[75] bridge,[78] and atop[12] sites. In contrast, we attribute the large conductance variation of **1d** to the lower binding energy of the CN–Au bond. Attempts to analyze the L regions in a similar way yielded a rather large distribution in the variation of the respective conductance values (Figure 4F), which correlates with the weaker interaction between the different molecules in these junctions and a larger variation in possible binding geometries. Moreover, we found that the conductance deviation of the M feature of PY is close to that of the H feature and clearly represents the characteristics of a single-molecule junction.

***I*–V_{bias} Curves from the MCBJ Measurements.** The high stability of the MCBJ setup offers the possibility of acquiring simultaneously I–V_{bias} curves during the slow opening and closing of molecular junctions.[79] Figure 5 displays typical traces

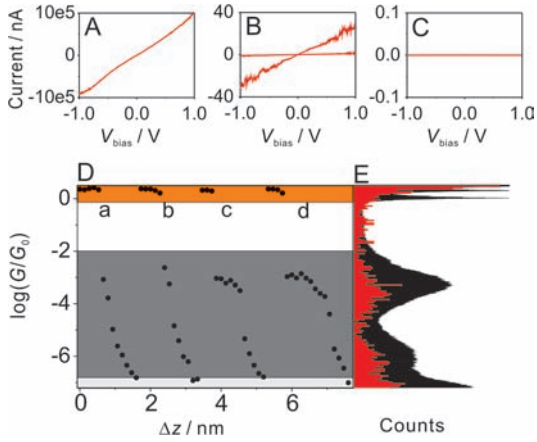

Figure 5. (A–C) Individual current–voltage curves of (A) gold–gold contact, (B) a molecular junction (H/L feature), and (C) tunneling current and noise level. (D) Conductance changes from the calculated slopes of I–V_{bias} curves in the four stretching processes. (E) Conductance histograms built from calculated slopes of I–V_{bias} measurement (red) and conductance–displacement measurement (black) on the MCBJ setup.

for the PY derivative **1a** recorded in different conductance ranges which represent Au–Au contacts (Figure 5A), the formation of a molecular junction (Figure 5B), and tunneling through the solvent (Figure 5C).

The corresponding zero bias conductances (Figure 5D) were calculated from the slopes of the linear parts of the I–V_{bias} curves in the range from −0.30 to +0.30 V at different stages during the stretching process. As shown in Figure 5D (where every data point represents the calculated conductance of one I–V_{bias} trace), I–V_{bias} curves initially exhibit the conductance of gold–gold contacts (orange area in panel D). Once the gold–gold contact is broken, up to 10 I–V_{bias} curves can be acquired in the H range of the molecular junction (dark gray area in panel D). The light gray area corresponds to traces recorded in the L range until approaching the noise level. We also note that the enhanced fluctuations at high bias voltages may lead to the breaking of molecular junctions before a complete elongation is reached. Examples are traces a and b in Figure 5D. The corresponding 1D log conductance histogram, as constructed from ~1000 individual data points, is displayed in Figure 5E. A peak at $10^{-3.4}$ G_0 represents the estimated most probable conductance, which, as expected, is in perfect agreement with the value $10^{-3.4}$ G_0 obtained from the conductance–displacement measurements in the MCBJ as well as in the STM-BJ configuration (Figure 2 and Table 1). Limitations in the setup for I–V_{bias} measurements at larger values of V_{bias} prevented us from obtaining reliable data in the lower conductance regions M and L (see the Supporting Information).

To perform a statistical analysis of the I–V_{bias} curves associated with the most probable conductances, we selected curves with $\log(G/G_0)$ in a range equal to the most probable value ±0.2 (from Table 1; in the case of PY, 3.3 ± 0.2 was chosen). The corresponding I–V_{bias} curves are shown in Figure 6.

Parts A–D of Figure 6 demonstrate clearly the existence of preferential conductance states. The most probable current as a function of bias was subsequently determined by fitting

dx.doi.org/10.1021/ja209844r | J. Am. Chem.Soc. 2012, 134, 2292–2304

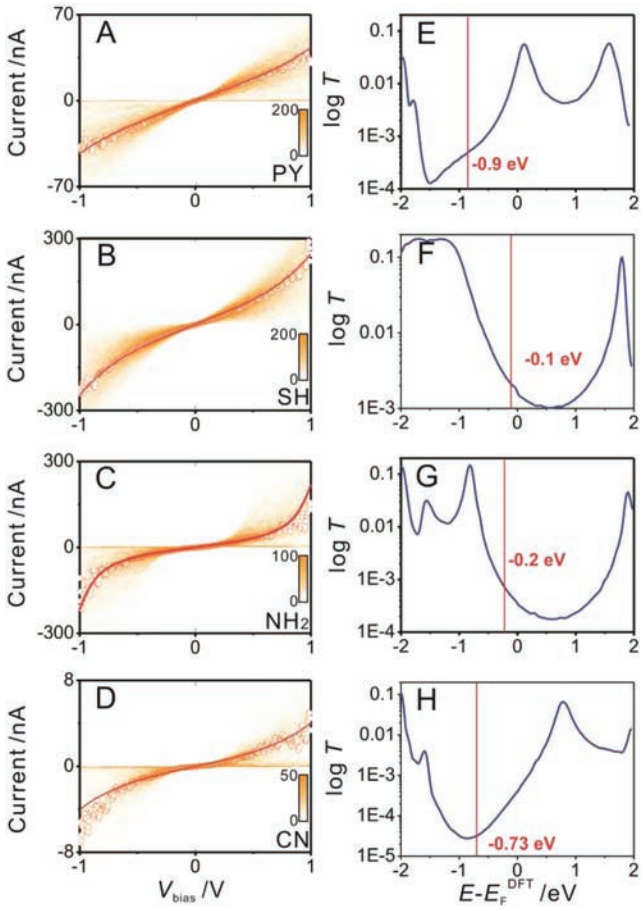

Figure 6. (A–D) Statistically obtained $I-V_{bias}$ traces from MCBJ measurements (open circles) and model fitting (solid line). (E–H) Computed transmission curves of the four tolane derivatives. For further details see the text and Supporting Information.

Gaussians to vertical sections of each bias voltage bin.[73] The resulting most probable $I-V_{bias}$ curve is plotted as an open-circle trace in Figure 6A–D. These curves are nonlinear, but show no characteristic resonance features. The experimentally determined most probable $I-V_{bias}$ curves are the basis for the comparison with ab initio generated transmission curves. Two factors control the conductance of a single-molecule junction in the nonresonant tunneling regime: (i) the position of the dominant transport channel relative to the metal Fermi level and (ii) the coupling of this level to the metal leads, resulting in a level broadening.[51] As shown in Figure 6, the $I-V_{bias}$ traces reveal distinct differences between the four tolane derivatives with different anchoring groups. For example, the **1a** (PY) trace is almost linear, which suggests that the true Fermi energy is located far from a molecular resonance peak. In contrast, the inflection points in the statistically constructed $I-V_{bias}$ traces of **1b–1d** suggest a closer position of the Fermi level to the main transport channel in the SH-, NH_2-, and CN-terminated molecular junctions.

DFT CALCULATIONS AND INTERPRETATION OF EXPERIMENTAL RESULTS

Binding Geometry and Binding Energy. To gain insight into the origin of measured conductances and $I-V_{bias}$ curves, we now compare experimental results with detailed DFT-based calculations. Initially we investigated the energetics of the four tolane derivatives bound to clusters of one (END1), two (END2), or three (END3) gold adatoms placed at the end of a Au(111) surface. These adatom clusters are shown in Figure S16 in the Supporting Information and were chosen to mimic the not flat surface of leads just after a monatomic contact breaks and snaps back.[77] The binding energies for each cluster and anchor group are shown in Table S1, Supporting Information.

We found that PY, NH_2, and CN bind selectively to undercoordinated gold sites regardless of the initially enforced bridge, hollow, or top positions. For the S anchor of the thiol (which remains after removal of the H from the SH moiety in all simulations), we found that, in the case of three adatoms, the hollow position is favored while, in the case of two adatoms, the bridge position is preferred. As shown in Figure S16 in the Supporting Information, compared to the terminal PY, NH_2, or CN end groups, the S anchoring site appears to have the least uniform binding geometry,[37,80] which contributes to a broadening of the conductance histograms.[36] Similar geometries have been reported[30,75,78,81] for related dithiolated aromatic wires.

Depending on the position of the anchor atom with respect to the atoms of a surface gold cluster (see Figure S16, Supporting Information), the Au–N bond lengths were computed as 0.212–0.214 and 0.209–0.211 nm for PY and CN, respectively. The Au–S bond lengths were obtained as 0.249–0.263 nm. We also observed that NH_2 binds less strongly to gold adatoms due to steric hindrance caused by the hydrogen atoms next to the nitrogen. Similarly, as demonstrated for 1,4-benzenediamine[39] and later for an entire family of aliphatic and aromatic diamines,[74] we found that this group favors binding to one gold adatom in a rather specific way as depicted in Figure S16. Depending on the coordination of the binding gold atom, the optimal Au–N bond length is computed to be 0.233–0.254 nm.

Table S1 in the Supporting Information reveals that the binding energies follow the sequence Au–S ≫ Au–PY > Au–CN > Au–NH_2. The thiol-based molecular junctions appear to be the most stable. Experimental support for this statement is provided by the observation that single-molecule junctions with Au–S contacts have the largest most probable plateau length (Table 2). Recent CP-AFM measurements[77,82–84] and first principle calculations[85,86] of bond rupture forces of Au–S (1.5 ± 0.2 nN), Au–PY (0.8 ± 0.2 nN), and Au–NH_2 (0.6 ± 0.2 nN) support our order of the binding energies. (For Au–Au the corresponding force is ∼1.5 nN.) The junction formation probabilities for both the main H states (Figure 3) and the L state (Supporting Information, Figure S13) follow the sequence PY > S > CN > NH_2, which is identical to the binding energy sequence, except that PY and S are reversed. This suggests that the binding energy plays a major role in determining the junction formation probability. Other factors affecting the junction formation include the ability of a molecule to migrate into the junction, which in the case of S may be reduced if the higher binding energy decreases the mobility of the anchor in the vicinity of the Au tip.

To compute electron transmission coefficients, electrodes with these surface clusters were attached to opposite ends of a molecule. Each electrode consisted of a cluster of adatoms on the surface, followed by two layers (a surface and a subsurface layer), each comprising 4 × 4 gold atoms. After geometry relaxation, current–voltage characteristics were calculated by connecting the subsurface layers to semiinfinite crystalline leads formed from 4 × 4 unit cells of gold atoms. We constructed the

dx.doi.org/10.1021/ja209844r | J. Am. Chem.Soc. 2012, 134, 2292–2304

initial geometries in the following way: First, we created perfectly symmetric contacts with three adatoms at both sides. We initially set the anchor atom (N for PY and CN, S for thiol) around top, bridge, and hollow positions. For NH_2 we initially placed the nitrogen atom in top and bridge positions, so that the hydrogen atoms pointed away from the gold adatoms. We performed geometry optimization of these initial systems with several different lead−molecule−lead distances and chose the energetically most favorable distances to determine the optimal molecule length L_m (Table 2). At this optimal distance, we systematically removed adatoms from each electrode and again performed geometry optimizations. The energy minimization allowed the molecule and the adatoms to relax their geometries while the gold layers were kept fixed. We used a double-ζ polarization (DZP) basis set and a generalized gradient approximation (GGA) exchange correlation functional with a 0.02 eV/Å force tolerance and applied periodic boundary conditions in all directions. Examples of optimal geometries for different numbers of surface adatoms are illustrated in Figure S17 in the Supporting Information.

Length of the Molecular Junctions. DFT calculations revealed the following values of an optimal length L_m of the four molecular junctions in the preferred binding geometries with three adatoms on both electrodes: 1.14 nm (PY), 1.48 nm (SH), 1.43 nm (NH_2), and 1.70 nm (CN) (Table 2).

The data in Table 2 demonstrate that the experimental absolute displacements in the high-conductance regions, $z^{H*} = \Delta z^{H*} + \Delta z_{corr}$, for PY **1a** ($z^{H*} = 1.2 \pm 0.2$ nm compared to $L_m = 1.14$ nm) and SH **1b** ($z^{H*} = 1.4 \pm 0.4$ nm compared to $L_m = 1.48$ nm) are close to L_m, suggesting that the junctions break when the molecules are being straightened. However, for the NH_2-substituted tolane **1c** ($z^{H*} = 1.2 \pm 0.3$ nm compared to $L_m = 1.43$ nm) and the CN-substituted tolane **1d** (1.1 ± 0.4 nm compared to 1.70 nm), z^H is lower than L_m, suggesting that the high-conductance junctions break before a fully stretched configuration is reached. This observation is attributed to the stability of the junctions. We note that the CN-substituted tolane **1d** shows only one conductance state (H). In contrast, for **1a** to **1c**, the histograms in Figures 2 and 3 and their analysis show that a certain number of initially formed traces with H features transform into configurations representing an L state. An additional M state is observed for the special case of **1a** (PY). We also estimate the most probable junction lengths in the L state (Table 2). The corresponding values of $\Delta z^{L*} + \Delta z_{corr}$ for **1a** (1.3 ± 0.2 nm) and in particular **1b** (1.7 ± 0.4 nm) appear to be clearly larger than L_m at 1.14 and 1.48 nm, respectively. This trend suggests a more complex evolution of the low-conductance state, which might involve the elongation of the contact region beyond the equilibrium state,[30] the pulling out of gold adatoms,[55,56,59] or the formation of intermolecular stacking assemblies[21] before complete breaking of the junction occurs. The case of the PY derivative **1a** is special because the transition of the H states into the low-conductance region occurs either directly or via an M state.

Simulation of the Configuration Evolution during Stretching. The observation (Figure 4) that the most probable conductance decreases during the pulling process indicates that molecular junctions evolve through a series of geometries as the electrode separation increases. To gain insight into the evolution of the junctions, we performed DFT-based simulations of a pulling curve for each of the tolanes **1a**−**1d**. As an initial configuration we started with an "extended molecule" formed by placing a six-atom gold pyramid at each end of the molecule (see Figure S17 in the Supporting Information). To follow the evolution of the junction, we generated a series of geometries with different electrode separations, which we defined to be the distance between the first 4 × 4 gold atomic layers at both sides. Initially. the distances between the pyramid peaks were smaller (~0.6 nm) than the molecular lengths and the optimized molecules were positioned approximately symmetrically next to the pyramids (later we refer to this as a SIDE configuration). To simulate the evolution of a junction, we introduced a classical Morse potential between the anchor and the gold atoms in the pyramids and hard wall potentials between the rest of the atoms (for more details see the Supporting Information). Then we performed a classical molecular dynamics simulation of the junction development with a rigid molecule and fixed gold pyramids in which only the position and orientation of the molecule relative to the pyramid varied. The Morse potential is intended to model the attachment of the molecule to the gold pyramids, and the hard wall was introduced to avoid unrealistic collisions of atoms. At each simulation step we changed the electrode separation distance by 0.04 nm and classically optimized the structure. The simulation started with a few steps of compression to decrease the gap between the gold pyramids to approach the snapback distance, which was estimated from experiments to be ~0.5 nm. From this point we simulated the stretching process of the molecular junction by increasing the distances until the molecular junction was completely broken. The sole purpose of this classical simulation was to generate a series of hypothetical initial geometries for the further DFT geometry optimization in which only the gold layers were kept fixed. Therefore, a realistic junction geometry was formed under different electrode separation constraints.

During the simulation we found that only the constrained space caused a large compression that bends the molecules significantly, which reflects the strong stiffness and rigidity of the molecules. The stiffness of the molecules introduces an extra constraint on the anchors at the two ends that limits the possibilities of forming optimal bonds with the anchors. Therefore, at the early stages of compression, the anchors are less important than the backbone of the molecule. Figure 7 shows the development of the junctions.

Transmission Curves and Most Probable Junction Conductances. After obtainment of the junction geometry at each stage in the stretching process, we then used the underlying DFT mean-field Hamiltonian to compute the electrical conductance. In an attempt to rationalize the experimentally observed trends, we calculated the quantum mechanical electron transmission coefficients for the series of relaxed geometries using a combination of the DFT-generated Hamiltonian (SIESTA) and the SMEAGOL package. The conductance was then obtained from the electron transmission coefficient $T(E)$, evaluated at the Fermi energy $E = E_F$.

DFT does not usually predict correctly the alignment of the frontier molecular energy levels in the junction relative to the Fermi energy, which results in too high conductance values. To overcome this deficiency, self-energy and screening corrections are required.[42,87] However, these corrections are typically obtained for locally optimal configurations in vacuum between rather flat contacts, which is not the case in our simulations. Furthermore, our current experiments are carried out at room temperature in a solution containing typically a 0.1 mM concentration of the tolane molecules. The correction depends sensitively on the precise coordination of the bridging gold

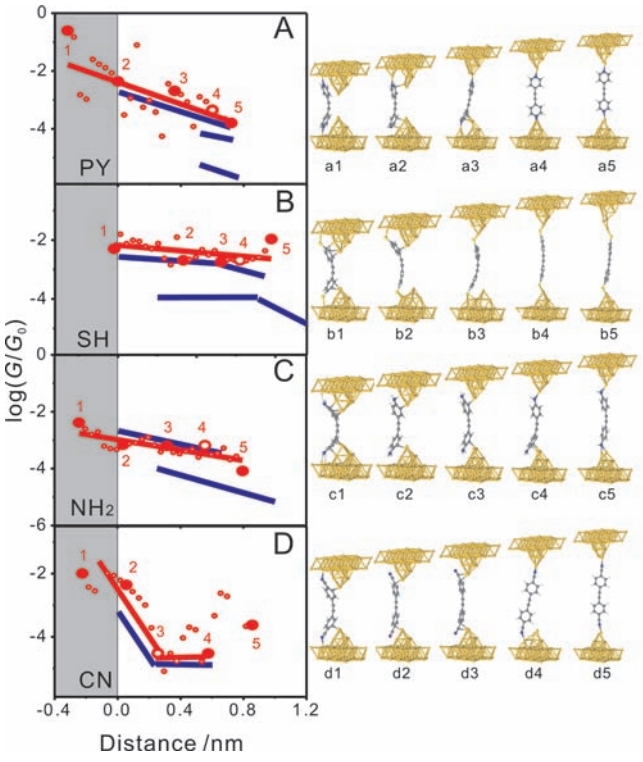

Figure 7. Experimentally measured conductance decay (blue line) and simulated stretching curves (red points) and their linear fits (red line) for PY (A), SH (B), NH_2 (C), and CN (D) together with examples of junction configurations at selected points along the curves. The red hollow circles indicate the points used to determine the Fermi energy.

atom, on the relative strengths of binding to the two gold electrodes, and on the position and orientation of the image–charge plane.[41] In view of these uncertainties, we adopted a more empirical approach to locating E_F. We located the relative positions of the dominant conductance channel (HOMO or LUMO) with respect to the Fermi energy by comparing DFT/SMEAGOL-computed current–voltage characteristics with experimentally measured I–V_{bias} curves (for details see the Supporting Information).

The comparison between experiment and theory involves measuring the I–V_{bias} characteristics of samples corresponding to the most probable high conductances (Table 2 and data points indicated in Figure 3A–D) at the corresponding most probable values of the electrode separation $\Delta z^{H*} + \Delta z_{corr}$ and $\Delta z^{L*} + \Delta z_{corr}$ (see Figure 3E–H for H and the Supporting Information for L). Subsequently, we computed the I–V_{bias} characteristics of the junction with this separation for a range of Fermi energies E_F in the vicinity of the DFT-predicted value. Those values of E_F were selected which gave the closest agreement with the corresponding experimental data. Figure 6 displays the I–V_{bias} curves recorded at the most probable conductance and gap separation in the high-conductance range (A–D), the junction geometry after relaxation, and the computed transmission curves (E, F) for **1a**–**1d**. The fitted positions of the adjusted values of E_F are indicated by the vertical lines. The corrections in E_F are −0.9 eV (PY), −0.1 eV (SH), −0.2 eV (NH_2), and −0.73 eV (CN). The empirical correction indicates that the transport through molecular junctions of **1a** (PY) and **1d** (CN) is due to nonresonant tunneling through the tails of the respective LUMO state. This is in agreement with results reported for related molecules from conductance and thermopower measurements.[13,42,45] In particular, we notice that an ab initio correction of the LUMO orbital energy in **1a** (PY) relative to E_F resulted in 1.56 eV, which compares reasonably with our empirical correction of 0.9 eV. This agreement supports the reliability of our current strategy. Transport through junctions of **1b** and **1c** appears to proceed via the tail of the nearby HOMO state. This result is also supported by published conductance and thermopower studies with structurally related molecules.[40,69,88] The average relative Fermi level values as obtained from both sets of I–V_{bias} measurements were then assumed to be independent of the electrode separation and were used to calculate the conductances in all stretching traces.

To fit to the most probable high-conductance I–V_{bias} curves of Figure 6, with electrode separations $\Delta z^{H*} + \Delta z_{corr}$, it was necessary to multiply the computed electron transmission coefficients by a scale factor A. This factor accounts for deficiencies in DFT, such as the absence of van der Waals interactions, which would increase the distance between the anchors and gold electrodes and thereby decrease the conductance. The same value of $A = 0.18$ was used for each of the four molecules. The conductance of the molecular junction was calculated (with the corrected Fermi energy) after each pulling step to construct the simulated stretching traces. Figure 7 summarizes the data and shows selected optimized junction geometries at various stages of the pulling process. The red hollow circles indicate the points used to determine the Fermi energy. These stretching distances correspond to the most probable (log) conductances obtained experimentally. The experimentally measured I–V curves at these points are compared with the theoretical I–V curves obtained at the same stretching distance. This comparison is carried out for each of the four molecules, and the four Fermi levels and a single common scaling parameter are adjusted to yield a best fit. (Further details are included in the Supporting Information.) The overall trends of the simulated curves in the H region, such as the evolution of plateaus upon stretching and their slopes, are in good agreement with the experimental data. The decay in the simulated conductances at larger displacements also provides clear evidence for the experimentally observed transition toward the low-conductance states for **1a** (PY), **1b** (SH), and **1c** (NH_2) before a complete junction rupture. The simulated curves reveal that the conductance plateaus are the result of continuous transitions between many conformations and junction geometries.

In the following we address specific details of the simulated traces. At distances shorter than the snapback (gray area in Figure 7), the gap size is significantly smaller than the molecular length. The artificially compressed molecules (labeled a1–d1 in Figure 7) bind directly via their anchoring groups to gold surface sites with the aromatic ring close to the gold pyramids, which gives rise to rather high conductance values not accessible in the real experiments. Upon stretching the junctions (to configurations labeled a2–d2 in Figure 7), the coordination with the smooth Au(111) surface appears to break, and an exclusive SIDE configuration is established, which is controlled by the ring–pyramid interaction. Moreover, for PY and NH_2 the carbon atoms in the ring showed preference over the anchor atoms. The typical distances for Au–C were found as ∼0.24 and ∼0.26 nm, whereas at the same time the distances between the nitrogen and the closest gold atom were around ∼0.29 and ∼0.3 nm, respectively, which are 0.08 and 0.05 nm larger than the optimal bond length calculated

dx.doi.org/10.1021/ja209844r | J. Am. Chem.Soc. 2012, 134, 2292–2304

between the anchor and gold. This shows that the ring makes a significant contribution to the binding and that the presence of the ring decreases the contribution to binding from the anchor group. The corresponding conductances are still rather high due to wide resonance peaks in the transmission (Supporting Information). Only the thiol of **1b** appears to interact stronger with the gold sites than the aromatic ring. In this case, the estimated Au−S distances of ∼0.25 nm are close to their optimal bond length. As the tip is further retracted (through configurations a3−d3 toward configurations a4−d4 of Figure 7), the tolanes **1a**, **1c**, and **1d** slowly slide down the side of the tip until the gap becomes large enough and the respective anchoring groups bind with undercoordinated gold atoms at the apex. Typically this occurs in an asymmetric manner. First, one anchor attaches to the apex atom, and subsequently the other follows. Developing asymmetry causes a decrease of conductance. The conductance in the END positions (Supporting Information, section 5.1) appears to be rather insensitive to the specific coordination site of the adatom on the gold surface underneath. In the case of **1b**, the sulfur−gold binding sites translocate either via a hopping-type place exchange or an alternative surface diffusion mechanism along the sides of the pyramid into a final atop position. This process also involves higher coordinated sites such as bridge and atop geometries. Compared to the other anchoring groups, the surface migration of the sulfur−gold sites involves major restructuring of the contacts. This is also reflected in the simulated data, where we found that the conductance variations in junctions of **1b** (SH) are much higher than those of **1a** (PY), **1c** (NH_2), or **1d** (CN), in agreement with our experimental observations (Figure 4). In all cases, a final top-site configuration is reached (configurations a5−d5 in Figure 7) by all four molecules in the simulated traces, giving rise to lower conductances due to a decreasing coupling between the anchoring group and the leads or interaction between molecules. Interestingly, the CN−Au junction breaks immediately, giving rise to the shortest simulated plateaus. This anchor has the weakest influence on the gold pyramid. The typical Au−N (NC) lengths were found to be ∼0.32 nm for shorter electrode separations, and also the ring approaches the pyramid with an average Au−C distance of ∼0.26 nm. A possible reason for the early junction break is the long and stiff CN anchor that prevents a strong ring−pyramid coupling.

A small elongation of the equilibrium Au−N(NH_2) bond (as compared to an upright position of the extended molecule without constraints in the gap width) is observed before rupture, which indicates the appearance of a long conductance feature. The elongations of the Au−Au−PY and Au−Au−S bonds are much longer, which even leads to the pulling out of chainlike gold atoms in the latter case (configuration b5 in Figure 7). The typical heights of the pyramids on the surface, as measured from the surface plane at the moment of breaking, are around ∼0.5 nm for PY and NH_2. However, in the case of SH, we obtain ∼0.7 nm. This result rationalizes the experimentally observed trend for SH having a characteristic distance much longer than the molecular length L_m. The decreasing slopes in the simulated conductance traces of **1a** and **1b** clearly show the evolution of the L state. A separate M state, as seen in the experimental observations of **1a** (PY), could be detected. These data show that the distance over which the four different types of molecular junctions could be stretched reveals the sequence **1d** < **1c** < **1a** < **1b**, in agreement with the experimental data. We also notice that the anchoring groups influence the slope in the H regime (Figure 7). The experimentally observed trend **1d** < **1b** < **1c** < **1a** is in good agreement with the simulated data.

The above simulations demonstrate that, in principle, fully stretched molecular junctions can be formed between the two gold leads in an STM-BJ or an MCBJ experiment. However, the main conductance features in the 1D and 2D histograms as experimentally observed represent primarily the statistical average of the higher conductance (involving SIDE or lower stretched top sites) configurations. Thermal vibrations and low binding energies, such as in the case of Au−N(NH_2) and Au−N(CN) configurations, lead to breaking events before a fully stretched configuration is formed. As a consequence, the experimentally observed most probable conductance very seldom represents the configuration of an upright oriented extended molecule.

CONCLUSION

We have systematically compared four different anchoring groups in a series of tolane derivatives and observed the following trends: First, from the conductance measurements in both MCBJ and STMBJ configurations, we found that PY (**1a**), SH (**1b**), and NH_2 (**1c**) showed relatively high conductances. Second, on the basis of an analysis of the conductance−displacement traces, PY and SH revealed statistically higher junction formation probabilities as well as molecular junction stabilities. This result is attributed to variety in the binding geometries and the higher binding energy. Third, we further analyzed the conductance decay and conductance variation in the stretching traces. We found that PY and NH_2 showed the smallest conductance fluctuations over the entire stretching process.

We also note that the chemical inertness of the PY and CN anchors is rather attractive, since they are stable under ambient conditions, and no protection group is needed. The SH moiety attached to an aromatic backbone is not stable in the presence of oxygen and thus requires a protection group and in situ deprotection in an inert atmosphere before the start of the conductance measurements.[89] Furthermore, it is well-known that aromatic amines are often used as antioxidants, because these compounds act as H atom donors in radical reactions due to relatively weak N−H bonds. Aromatic amines have low ionization potentials and rather weak N−H bonds. They can undergo oxidation reactions and hydrogen atom transfer reactions rather easily.[90,91] Moreover, the NH_2 group is sensitive to light.

To summarize, we have studied experimentally and theoretically charge transport through tolane derivatives connected to gold electrodes via four different anchoring groups. Comparable results for conductance−displacement measurements were obtained for both STM-BJ and MCBJ setups, which strengthens the experimental reliability of our single-molecule conductance measurements. According to the analysis of the conductance−displacement traces from the STM-BJ setup, PY exhibits the best anchoring performance of the four groups analyzed, with high conductance and 100% molecular junctions formed. This conclusion is also strongly supported by the theoretical calculations of the binding energy and binding geometry. Furthermore, current−voltage curves constructed for the most probable MCBJ molecular geometries provided access to estimate the relative positions of the molecular levels with respect to the Fermi level, which facilitated the simulation of the dynamic stretching curves.

dx.doi.org/10.1021/ja209844r | J. Am. Chem.Soc. 2012, 134, 2292−2304

Comparison between experiment and theory yields good agreement in the conductance decay of the molecular conductance plateaus and highlights the underlying atomic-scale complexity of the stretching curves, which reveal the role of the anchoring group in the evolution of the configuration of the single molecular junctions.

■ ASSOCIATED CONTENT

Supporting Information

Details of the molecular synthesis, the experimental setup and data analysis, and the DFT-type transport calculations (AVI). This material is available free of charge via the Internet at http://pubs.acs.org.

■ AUTHOR INFORMATION

Corresponding Author

c.lambert@lancaster.ac.uk; m.r.bryce@durham.ac.uk; thomas.wandlowski@dcb.unibe.ch

■ ACKNOWLEDGMENTS

This work was supported by the Swiss National Science Foundation (Grant 200021-124643, Nationales Forschungsprogramm (National Research Program) 62), European Commission (EC) FP7 Initial Training Network (ITN) "FUNMOLS" Project No. 212942, and the University of Bern. P.M.G. acknowledges Consejo Nacional de Ciencia y Tecnología (CONACyT), México (Grant 209297). C.J.L. acknowledges support from EPSRC and the FP7 ITN NanoCTM.

■ REFERENCES

(1) Tour, J. M. *Acc. Chem. Res.* **2000**, *33*, 791−804.
(2) Reed, M. A.; Zhou, C.; Muller, C. J.; Burgin, T. P.; Tour, J. M. *Science* **1997**, *278*, 252−254.
(3) Xu, B. Q.; Tao, N. J. J. *Science* **2003**, *301*, 1221−1223.
(4) Chen, F.; Hihath, J.; Huang, Z. F.; Li, X. L.; Tao, N. J. *Annu. Rev. Phys. Chem.* **2007**, *58*, 535−564.
(5) Donhauser, Z. J.; Mantooth, B. A.; Kelly, K. F.; Bumm, L. A.; Monnell, J. D.; Stapleton, J. J.; Price, D. W.; Rawlett, A. M.; Allara, D. L.; Tour, J. M.; Weiss, P. S. *Science* **2001**, *292*, 2303−2307.
(6) Andres, R. P.; Bein, T.; Dorogi, M.; Feng, S.; Henderson, J. I.; Kubiak, C. P.; Mahoney, W.; Osifchin, R. G.; Reifenberger, R. *Science* **1996**, *272*, 1323−1325.
(7) Repp, J.; Meyer, G.; Paavilainen, S.; Olsson, F. E.; Persson, M. *Science* **2006**, *312*, 1196−1199.
(8) Weibel, N.; Grunder, S.; Mayor, M. *Org. Biomol. Chem.* **2007**, *5*, 2343−2353.
(9) Cui, X. D.; Primak, A.; Zarate, X.; Tomfohr, J.; Sankey, O. F.; Moore, A. L.; Moore, T. A.; Gust, D.; Harris, G.; Lindsay, S. M. *Science* **2001**, *294*, 571−574.
(10) Fan, F. R. F.; Yang, J. P.; Cai, L. T.; Price, D. W.; Dirk, S. M.; Kosynkin, D. V.; Yao, Y. X.; Rawlett, A. M.; Tour, J. M.; Bard, A. J. *J. Am. Chem. Soc.* **2002**, *124*, 5550−5560.
(11) Venkataraman, L.; Klare, J. E.; Nuckolls, C.; Hybertsen, M. S.; Steigerwald, M. L. *Nature* **2006**, *442*, 904−907.
(12) Li, C.; Pobelov, I.; Wandlowski, T.; Bagrets, A.; Arnold, A.; Evers, F. *J. Am. Chem. Soc.* **2008**, *130*, 318−326.
(13) Mishchenko, A.; Zotti, L. A.; Vonlanthen, D.; Burkle, M.; Pauly, F.; Cuevas, J. C.; Mayor, M.; Wandlowski, T. *J. Am. Chem. Soc.* **2011**, *133*, 184−187.
(14) Moth-Poulsen, K.; Bjornholm, T. *Nat. Nanotechnol.* **2009**, *4*, 551−556.
(15) Haiss, W.; van Zalinge, H.; Higgins, S. J.; Bethell, D.; Hobenreich, H.; Schiffrin, D. J.; Nichols, R. J. *J. Am. Chem. Soc.* **2003**, *125*, 15294−15295.
(16) Kushmerick, J. G.; Holt, D. B.; Pollack, S. K.; Ratner, M. A.; Yang, J. C.; Schull, T. L.; Naciri, J.; Moore, M. H.; Shashidhar, R. *J. Am. Chem. Soc.* **2002**, *124*, 10654−10655.
(17) Dadosh, T.; Gordin, Y.; Krahne, R.; Khivrich, I.; Mahalu, D.; Frydman, V.; Sperling, J.; Yacoby, A.; Bar-Joseph, I. *Nature* **2005**, *436*, 677−680.
(18) Kergueris, C.; Bourgoin, J. P.; Palacin, S.; Esteve, D.; Urbina, C.; Magoga, M.; Joachim, C. *Phys. Rev. B* **1999**, *59*, 12505−12513.
(19) Reichert, J.; Ochs, R.; Beckmann, D.; Weber, H. B.; Mayor, M.; von Lohneysen, H. *Phys. Rev. Lett.* **2002**, *88*, 176804.
(20) Smit, R. H. M.; Noat, Y.; Untiedt, C.; Lang, N. D.; van Hemert, M. C.; van Ruitenbeek, J. M. *Nature* **2002**, *419*, 906−909.
(21) Wu, S. M.; Gonzalez, M. T.; Huber, R.; Grunder, S.; Mayor, M.; Schonenberger, C.; Calame, M. *Nat. Nanotechnol.* **2008**, *3*, 569−574.
(22) Lortscher, E.; Ciszek, J. W.; Tour, J.; Riel, H. *Small* **2006**, *2*, 973−977.
(23) Park, J.; Pasupathy, A. N.; Goldsmith, J. I.; Chang, C.; Yaish, Y.; Petta, J. R.; Rinkoski, M.; Sethna, J. P.; Abruna, H. D.; McEuen, P. L.; Ralph, D. C. *Nature* **2002**, *417*, 722−725.
(24) Osorio, E. A.; Bjornholm, T.; Lehn, J. M.; Ruben, M.; van der Zant, H. S. J. *J. Phys.: Condens. Matter* **2008**, *20*, 374121.
(25) Chen, J.; Reed, M. A.; Rawlett, A. M.; Tour, J. M. *Science* **1999**, *286*, 1550−1552.
(26) Slowinski, K.; Fong, H. K. Y.; Majda, M. *J. Am. Chem. Soc.* **1999**, *121*, 7257−7261.
(27) Haag, R.; Rampi, M. A.; Holmlin, R. E.; Whitesides, G. M. *J. Am. Chem. Soc.* **1999**, *121*, 7895−7906.
(28) Chiechi, R. C.; Weiss, E. A.; Dickey, M. D.; Whitesides, G. M. *Angew. Chem., Int. Ed.* **2008**, *47*, 142−144.
(29) Loertscher, E.; Cho, C. J.; Mayor, M.; Tschudy, M.; Rettner, C.; Riel, H. *ChemPhysChem* **2011**, *12*, 1677−1682.
(30) Zotti, L. A.; Kirchner, T.; Cuevas, J. C.; Pauly, F.; Huhn, T.; Scheer, E.; Erbe, A. *Small* **2010**, *6*, 1529−1535.
(31) Ranganathan, S.; Steidel, I.; Anariba, F.; McCreery, R. L. *Nano Lett.* **2001**, *1*, 491−494.
(32) Cheng, Z. L.; Skouta, R.; Vazquez, H.; Widawsky, J. R.; Schneebeli, S.; Chen, W.; Hybertsen, M. S.; Breslow, R.; Venkataraman, L. *Nat. Nanotechnol.* **2011**, *6*, 353−357.
(33) Mishchenko, A.; Abdualla, M.; Rudnev, A.; Fu, Y.; Pike, A. R.; Wandlowski, T. *Chem. Commun.* **2011**, *47*, 9807−9809.
(34) Pauly, F.; Viljas, J. K.; Cuevas, J. C.; Schoen, G. *Phys. Rev. B* **2008**, *77*, 155312.
(35) Jones, D. R.; Troisi, A. *J. Phys. Chem. C* **2007**, *111*, 14567−14573.
(36) Ulrich, J.; Esrail, D.; Pontius, W.; Venkataraman, L.; Millar, D.; Doerrer, L. H. *J. Phys. Chem. B* **2006**, *110*, 2462−2466.
(37) Muller, K. H. *Phys. Rev. B* **2006**, *73*, 045403.
(38) Roper, M. G.; Skegg, M. P.; Fisher, C. J.; Lee, J. J.; Dhanak, V. R.; Woodruff, D. P.; Jones, R. G. *Chem. Phys. Lett.* **2004**, *389*, 87−91.
(39) Venkataraman, L.; Klare, J. E.; Tam, I. W.; Nuckolls, C.; Hybertsen, M. S.; Steigerwald, M. L. *Nano Lett.* **2006**, *6*, 458−462.
(40) Quek, S. Y.; Venkataraman, L.; Choi, H. J.; Louie, S. G.; Hybertsen, M. S.; Neaton, J. B. *Nano Lett.* **2007**, *7*, 3477−3482.
(41) Dell'Angela, M.; Kladnik, G.; Cossaro, A.; Verdini, A.; Kamenetska, M.; Tamblyn, I.; Quek, S. Y.; Neaton, J. B.; Cvetko, D.; Morgante, A.; Venkataraman, L. *Nano Lett.* **2010**, *10*, 2470−2474.
(42) Quek, S. Y.; Kamenetska, M.; Steigerwald, M. L.; Choi, H. J.; Louie, S. G.; Hybertsen, M. S.; Neaton, J. B.; Venkataraman, L. *Nat. Nanotechnol.* **2009**, *4*, 230−234.
(43) Bagrets, A.; Arnold, A.; Evers, F. *J. Am. Chem. Soc.* **2008**, *130*, 9013−9018.
(44) Stadler, R.; Thygesen, K. S.; Jacobsen, K. W. *Phys. Rev. B* **2005**, *72*, 241401.
(45) Wang, C. S.; Batsanov, A. S.; Bryce, M. R.; Martin, S.; Nichols, R. J.; Higgins, S. J.; Garcia-Suarez, V. M.; Lambert, C. J. *J. Am. Chem. Soc.* **2009**, *131*, 15647−15654.
(46) Kim, B.; Beebe, J. M.; Jun, Y.; Zhu, X. Y.; Frisbie, C. D. *J. Am. Chem. Soc.* **2006**, *128*, 4970−4971.

(47) Chen, F.; Li, X.; Hihath, J.; Huang, Z.; Tao, N. *J. Am. Chem. Soc.* **2006**, *128*, 15874−15881.
(48) Schull, G.; Frederiksen, T.; Arnau, A.; Sanchez-Portal, D.; Berndt, R. *Nat. Nanotechnol.* **2011**, *6*, 23−27.
(49) Martin, C. A.; Ding, D.; Sorensen, J. K.; Bjornholm, T.; van Ruitenbeek, J. M.; van der Zant, H. S. J. *J. Am. Chem. Soc.* **2008**, *130*, 13198−13199.
(50) Kushmerick, J. G.; Whitaker, C. M.; Pollack, S. K.; Schull, T. L.; Shashidhar, R. *Nanotechnology* **2004**, *15*, S489−S493.
(51) Cuevas, J. C.; Scheer, E. *Molecular Electronics: An Introduction to Theory and Experiment*; World Scientific: Singapore, 2010.
(52) Noy, A. *Handbook of Molecular Force Spectroscopy*; Springer: New York, 2008.
(53) Park, Y. S.; Whalley, A. C.; Kamenetska, M.; Steigerwald, M. L.; Hybertsen, M. S.; Nuckolls, C.; Venkataraman, L. *J. Am. Chem. Soc.* **2007**, *129*, 15768−15769.
(54) Kamenetska, M.; Koentopp, M.; Whalley, A. C.; Park, Y. S.; Steigerwald, M. L.; Nuckolls, C.; Hybertsen, M. S.; Venkataraman, L. *Phys. Rev. Lett.* **2009**, *102*, 126803.
(55) Kruger, D.; Fuchs, H.; Rousseau, R.; Marx, D.; Parrinello, M. *Phys. Rev. Lett.* **2002**, *89*, 186402.
(56) Paulsson, M.; Krag, C.; Frederiksen, T.; Brandbyge, M. *Nano Lett.* **2009**, *9*, 117−121.
(57) Krüger, D.; Rousseau, R.; Fuchs, H.; Marx, D. *Angew. Chem., Int. Ed.* **2003**, *42*, 2251−2253.
(58) Wang, G. M.; Sandberg, W. C.; Kenny, S. D. *Nanotechnology* **2006**, *17*, 4819−4824.
(59) Konopka, M.; Turansky, R.; Reichert, J.; Fuchs, H.; Marx, D.; Stich, I. *Phys. Rev. Lett.* **2008**, *100*, 115503.
(60) Kim, Y.; Hellmuth, T. J.; Bürkle, M.; Pauly, F.; Scheer, E. *ACS Nano* **2011**, *5*, 4104−4111.
(61) Champness, N. R.; Khlobystov, A. N.; Majuga, A. G.; Schroder, M.; Zyk, N. V. *Tetrahedron Lett.* **1999**, *40*, 5413−5416.
(62) Nishimura, D.; Oshikiri, T.; Takashima, Y.; Hashidzume, A.; Yamaguchi, H.; Harada, A. *J. Org. Chem.* **2008**, *73*, 2496−2502.
(63) Dixon, S.; Whitby, R. J. *Tetrahedron Lett.* **2006**, *47*, 8147−8150.
(64) Liu, K.; Li, G.; Wang, X.; Wang, F. *J. Phys. Chem. C* **2008**, *112*, 4342−4349.
(65) Hong, W.; Valkenier, H.; Mészáros, G.; Manrique, D. Z.; Mishchenko, A.; Putz, A.; García, P. M.; Lambert, C. J.; Hummelen, J. C.; Wandlowski, T. *Beilstein J. Nanotechnol.* **2011**, *2*, 699−713.
(66) Rocha, A. R.; Garcia-Suarez, V. M.; Bailey, S.; Lambert, C.; Ferrer, J.; Sanvito, S. *Phys. Rev. B* **2006**, *73*, 085414.
(67) Rocha, A. R.; Garcia-Suarez, V. M.; Bailey, S. W.; Lambert, C. J.; Ferrer, J.; Sanvito, S. *Nat. Mater.* **2005**, *4*, 335−339.
(68) Soler, J. M.; Artacho, E.; Gale, J. D.; Garcia, A.; Junquera, J.; Ordejon, P.; Sanchez-Portal, D. *J. Phys.: Condens. Matter* **2002**, *14*, 2745−2779.
(69) Mishchenko, A.; Vonlanthen, D.; Meded, V.; Burkle, M.; Li, C.; Pobelov, I. V.; Bagrets, A.; Viljas, J. K.; Pauly, F.; Evers, F.; Mayor, M.; Wandlowski, T. *Nano Lett.* **2010**, *10*, 156−163.
(70) Yanson, A. I.; Bollinger, G. R.; van den Brom, H. E.; Agrait, N.; van Ruitenbeek, J. M. *Nature* **1998**, *395*, 783−785.
(71) Velizhanin, K. A.; Zeidan, T. A.; Alabugin, I. V.; Smirnov, S. *J. Phys. Chem. B* **2010**, *114*, 14189−14193.
(72) Xing, Y.; Park, T.-H.; Venkatraman, R.; Keinan, S.; Beratan, D. N.; Therien, M. J.; Borguet, E. *J. Am. Chem. Soc.* **2010**, *132*, 7946−7956.
(73) Widawsky, J. R.; Kamenetska, M.; Klare, J.; Nuckolls, C.; Steigerwald, M. L.; Hybertsen, M. S.; Venkataraman, L. *Nanotechnology* **2009**, *20*, 434009.
(74) Hybertsen, M. S.; Venkataraman, L.; Klare, J. E.; Cwhalley, A.; Steigerwald, M. L.; Nuckolls, C. *J. Phys.: Condens. Matter* **2008**, *20*, 374115.
(75) Haiss, W.; Wang, C. S.; Grace, I.; Batsanov, A. S.; Schiffrin, D. J.; Higgins, S. J.; Bryce, M. R.; Lambert, C. J.; Nichols, R. J. *Nat. Mater.* **2006**, *5*, 995−1002.
(76) Martin, S.; Grace, I.; Bryce, M. R.; Wang, C.; Jitchati, R.; Batsanov, A. S.; Higgins, S. J.; Lambert, C. J.; Nichols, R. J. *J. Am. Chem. Soc.* **2010**, *132*, 9157−9164.
(77) Agrait, N.; Yeyati, A. L.; van Ruitenbeek, J. M. *Phys. Rep.* **2003**, *377*, 81−279.
(78) Markussen, T.; Schioumltz, J.; Thygesen, K. S. *J. Chem. Phys.* **2010**, *132*, 224104.
(79) Lortscher, E.; Weber, H. B.; Riel, H. *Phys. Rev. Lett.* **2007**, *98*, 176807.
(80) Tomfohr, J.; Sankey, O. F. *J. Chem. Phys.* **2004**, *120*, 1542−1554.
(81) Leng, Y. S.; Krstic, P. S.; Wells, J. C.; Cummings, P. T.; Dean, D. J. *J. Chem. Phys.* **2005**, *122*, 244721.
(82) Xu, B. Q.; Xiao, X. Y.; Tao, N. J. *J. Am. Chem. Soc.* **2003**, *125*, 16164−16165.
(83) Frei, M. F. M.; Aradhya, S. V.; Koentopp, M.; Hybertsen, M. S.; Venkataraman, L. *Nano Lett.* **2011**, *11*, 1518−1523.
(84) Pobelov, I. V.; Meszaros, G.; Yoshida, K.; Mishchenko, A.; Gulcur, M.; Bryce, M. R.; Wandlowski, T *J. Phys.: Condens. Matter* **2011**, in press.
(85) Velez, P.; Dassie, S. A.; Leiva, E. P. M *Phys. Rev. Lett.* **2005**, *95*, 045503.
(86) Velez, P.; Dassie, S. A.; Leiva, E. P. M *Phys. Rev. B* **2010**, *81*, 235435.
(87) Mowbray, D. J.; Jones, G.; Thygesen, K. S. *J. Chem. Phys.* **2008**, *128*, 111103.
(88) Bratkovsky, A. M.; Kornilovitch, P. E. *Phys. Rev. B* **2003**, *67*, 115307.
(89) Valkenier, H. V. H.; Huisman, E. H.; van Hal, P. A.; de Leeuw, D. M.; Chiechi, R. C.; Hummelen, J. C. *J. Am. Chem. Soc.* **2011**, *133*, 4930−4939.
(90) Oldfield, L. F.; Bockris, J. O. M. *J. Phys. Chem.* **1951**, *55*, 1255−1274.
(91) Jacob, J. A.; Naumov, S.; Biswas, N.; Mukherjee, T.; Kapoor, S. *J. Phys. Chem. C* **2007**, *111*, 18397−18404.